HOKKAIDO UNIVERSITY

Title	Phase unwrapping for noisy phase map using localized compensator
Author（s）	Tomioka，Satoshi；Nishiyama，Shusuke
Citation	Applied Optics，51（21），4984-4994 https：doi.org10.1364AO.51.004984
Issue Date	2012-07-20
Doc URL	http：hdl.handle.net211549884
Rights	© 2012 Optical Society of America
Type	article
File Information	AO51-21-4984-4994.pdf

Instructions for use

Phase unwrapping for noisy phase map using localized compensator

Satoshi Tomioka* and Shusuke Nishiyama

Faculty of Engineering, Hokkaido University, Kita 13 Nishi 8, Kita-ku, Sapporo, Hokkaido 060-8628, Japan

*Corresponding author: tom@qe.eng.hokudai.ac.jp

Phase unwrapping for a noisy image suffers from many singular points. Singularity-spreading methods are useful for the noisy image to regularize the singularity. However, the methods have a drawback of distorting phase distribution in a regular area that contains no singular points. When the singular points are confined in some local areas, the regular region is not distorted. This paper proposes a new phase unwrapping algorithm that uses a localized compensator obtained by clustering and by solving Poisson's equation for the localized areas. The numerical results demonstrate that the proposed method can improve the accuracy compared with other singularity-spreading methods. © 2012 Optical Society of America

OCIS codes: 030.4280, 090.2880, 100.3175, 100.5088, 110.5086, 120.5050.

1. Introduction

Interferometers or in-line holography techniques are widely applied for the purpose of quantitative measurement of two-dimensional optical distance distribution. In these systems, fringe patterns are measured by digital devices such as CCD cameras, then phase information is retrieved using Fourier domain filtering [1–3] or phase shift techniques [2,4,5]. The retrieved phase is a principal value of phase that is bounded between $(-\pi, \pi]$. Phase unwrapping is applied to unfold the principal value to the unbounded phase.

When a wrapped phase map satisfies the sampling theorem, phase unwrapping can be readily achieved from one point to the other point by accumulating the phase differences (phase gradient). Ideally, the unwrapped results are independent of the accumulation (integration) path. In other words, the integral of phase gradient along any loop is identical to zero. However, in the case where the experimental data are noisy, i.e., some portions in the data area do not satisfy the sampling theorem, an integral enclosing a certain point may not vanish. This point is called "singular point."

In order to solve inconsistencies caused by singular points, many phase unwrapping algorithms have been proposed in the past. When we focus on the algorithms that handle the singular points directly, they are classified into two types according to the nature of the unwrapped result. (The classification, including the methods that do not handle the singular points such as denoising methods, is also shown in [6].)

The first type is path-following methods using the branch-cut method [7–13]. In these algorithms, the unwrapping operation is carried out along paths of successive pixels, where the paths are taken to avoid inconsistent pixels. When the signal-to-noise ratio of an original wrapped phase is relatively high (not noisy), the algorithms can unwrap the wrapped phase successfully. The effect of inconsistencies is distributed in a local narrow region. However, in the case of noisy data, it sometimes creates unnatural and unintended gaps of unwrapped phase with the theoretical error with the multiples of 2π. This is a serious problem for the quantitative evaluation of two-dimensional optical distance.

The other type of algorithm spreads the effect of a singular point to the whole area of image data.

The method based on least-square approaches [14–20], the singularity-spreading phase unwrapping method [21], and the methods using a rotational compensator [22,23] are categorized into this type. These methods do not introduce the unnatural gaps; however, they distort regular regions that contain no singular points.

In this paper, we propose a phase unwrapping method using a new compensator called a "localized compensator." The localized compensator can regularize the inconsistency only in the local area around the singular points. Since the original regular area outside the local area is not distorted, the method using the localized compensator is more accurate than the others.

This paper is organized as follows. Section 2 introduces the meaning of singular point, the regularization by compensator, and the concept of the localized compensator. In addition, it is shown that the localized compensator is equivalent to a certain flux density distribution satisfying Poisson's equation with a Neumann condition. Section 3 shows the clustering algorithm that determines local area containing singular points. The method to solve the flux for the Poisson's equation is shown in Section 4. The applicability of the proposed algorithm is demonstrated by a numerical simulation and two actual data in Section 5. Finally, conclusion is given in Section 6.

2. Phase Unwrapping by Compensator

A. Singularity in Phase Unwrapping

When we consider that true phase distribution, ϕ, is a continuous scalar function, the integral of the gradient along closed path vanishes because $\nabla \times \nabla \phi = 0$. However, we can only obtain the wrapped phase, ϕ_w, that is bounded within $(-\pi, \pi]$ because of the restriction of the measurement system. Moreover, ϕ_w is only measured at discrete points (nodes). The wrapping operator, $\mathcal{W}\{\cdot\}$, can be defined by using a function $\mathrm{Int}[\cdot]$ that returns the nearest integer as follows:

$$\phi_w = \mathcal{W}\{\phi\} \triangleq \phi - \mathrm{Int}\left[\frac{\phi}{2\pi}\right]2\pi. \tag{1}$$

A wrapped phase difference $(g \cdot \hat{s})$ of two adjoining nodes (r and $r' = r + \hat{s}\Delta l$) is defined and transformed as follows:

$$g \cdot \hat{s} \triangleq \frac{1}{\Delta l}\mathcal{W}\{\Delta\phi_w\} = \frac{1}{\Delta l}\left(\Delta\phi - \mathrm{Int}\left[\frac{\Delta\phi}{2\pi}\right]2\pi\right)$$
$$= \nabla\phi \cdot \hat{s} - \mathrm{Int}\left[\frac{\Delta\phi}{2\pi}\right]\frac{2\pi}{\Delta l}, \tag{2}$$

where both g and $\nabla\phi$ are constant on the segment between r and r'.

If the phase distribution is sampled frequently, i.e., the sampling theorem is satisfied, since the $\Delta\phi$ does not exceed a half-cycle, $\mathrm{Int}[\Delta\phi/2\pi] = 0$, and g is

considered as $\nabla\phi$. As a result, the phase at r', i.e., $\phi(r')$, can be unwrapped using g from a reference phase at r, i.e., $\phi(r)$.

In contrast, if the sampling theorem is not satisfied, the $\mathrm{Int}[\Delta\phi/2\pi]$ is a nonzero integer number. The smallest loop, named "elementary loop," consists of four segments with 2-by-2 square nodes. An integral of the elementary loop can take $2\pi m$, where $m \in \{0, \pm 1\}$ [24], in which m is called residue when $m = 1$ or $m = -1$ and m is not a residue when $m = 0$. In the case of an arbitrary closed path, C, since the path is considered as a boundary of the region that is connected with subregions of elementary loops, the integral of C is expressed as

$$\oint_C g \cdot \hat{s}\mathrm{d}l = 2\pi\sum_k m_k. \tag{3}$$

B. Regularization by Compensator

According to Helmholtz's theorem [25], any vector can be given by a sum of two kinds of vectors: an irrotational vector that is a gradient of an arbitrary scalar function and a rotational vector that is a rotation of a divergence free vector function. Since the unwrapped phase ϕ must be a scalar field, the difference vector of wrapped phase g in Eq. (2) satisfies the following equation using the divergence free vector function, A:

$$g = \nabla\phi + \nabla \times A, \tag{4}$$

$$\nabla \cdot A = 0. \tag{5}$$

By applying Stokes' theorem to an integral of the rotation of Eq. (4) over a domain enclosed by a path C and by comparing the result with Eq. (3), we can obtain the following relations:

$$c \triangleq -\nabla \times A, \tag{6}$$

$$\oint_C (g + c) \cdot \hat{s}\mathrm{d}l = 0, \tag{7}$$

$$\oint_C c \cdot \hat{s}\mathrm{d}l = -2\pi\sum_k m_k. \tag{8}$$

Equation (7) shows that the integral of $g + c$ from one point to the other point does not depend on the path, and $g + c$ is not singular anymore. We name the c "compensator." Once the c that satisfies Eq. (8) is found, we can carry out phase unwrapping successively using the following integration or accumulation of compensators:

$$\phi(r) = \phi(r_0) + \int_{r_0}^{r} g \cdot \hat{s}\mathrm{d}l + \int_{r_0}^{r} c \cdot \hat{s}\mathrm{d}l. \tag{9}$$

Most of past studies did not state the concept of compensator explicitly. However, the compensator

$C_1 \simeq 0.352 \quad C_2 \simeq 0.148 \quad C_3 \simeq 0.108$
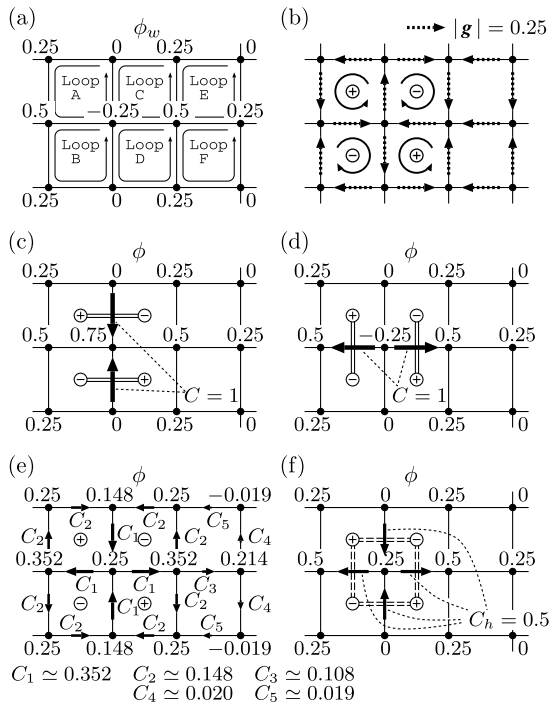$C_4 \simeq 0.020 \quad C_5 \simeq 0.019$

Fig. 1. Regularization of a quadrupole singularity: (a) original wrapped phase in the range $(-0.5, 0.5]$ cycles; (b) differences between adjoining nodes shown with dashed arrows and singular points; (c) unwrapped phase by horizontal branch cuts; (d) unwrapped phase by vertical branch cuts; (e) unwrapped phase by rotational compensators; (f) unwrapped phase by localized compensators. In (c) and (d), the double lines indicate the branch cuts. From (c) to (f) the solid arrows indicate the compensators of which widths and lengths indicate magnitude.

is used in many phase unwrapping methods. Approaches to remove singularities in phase unwrapping are categorized into two types.

Figure 1 demonstrates an example of regularization by a branch-cut method and by a use of a *rotational compensator* [22] as a typical singularity-spreading method. In this example, four singular points are placed within six elementary loops (Loops A to F). The wrapped phase, ϕ_w, is shown beside the nodes in Fig. 1(a).

Although all wrapped differences on segments $g(r, r')$ have the same magnitude with a quarter cycle, the directions of them are different. These are shown with the dashed arrows in Fig. 1(b), and the head of each arrow shows the direction of increase. Loop A, B, C, and D each contain singular points with residues since the closed integral along the loop is equal to $+1$ or -1 cycle.

Both Fig. 1(c) and 1(d) show the regularization by the method based on the branch cut. Every branch cut is put between a pair of a positive singular point and a negative singular point. In this example, there are two ways to put the branch cuts: a horizontal placement and a vertical placement. When a segment crosses each branch cut, a compensator with a value of one cycle is added to the wrapped difference in the phase unwrapping process. A difference between the unwrapped results of two cases is only found

at the central node of four singular points as the phases of 0.75 and −0.25 cycles. The difference is just one cycle. The unwrapped phase strongly depends on the choice of branch cuts. This is a drawback of the branch-cut methods.

Figure 1(e) shows an unwrapped phase using the rotational compensator. Since the detailed computation of the rotational compensator is found in [22], we focus here only on the nature of the rotational compensator. The unwrapped phase at the central node of four singular points is 0.25. This value is equal to the average of the unwrapped results of two branch-cut methods shown in Fig. 1(c) and 1(d). It means that the drawback of the unwrapped phase ambiguity in the branch-cut method is reduced by the rotational compensator method. However, the differences at the other nodes are found due to the effect of the compensator. Furthermore, other segments belonging to the regular loops such as Loops E and F have nonzero compensators to keep the loops' regularity. The amplitude of compensator decreases as the distance from every singular point increases; however, it spreads over the whole region; i.e., the compensation by rotational compensator (RC) distorts in the distant region. This is a drawback of the RC method. This distortion is also found in other phase unwrapping approaches of the singularity-spreading type.

Figure 1(f) shows an approach using localized compensators, which is the proposed approach in this article. Four quasi-branch-cuts are placed between positive and negative singular points. When a segment crosses the quasi-branch-cut, a compensator with a half-cycle is applied in this example. In this approach, the unwrapped phase at the central node of singular points is equal to that of the RC approach. Furthermore, there is no distortion in the regular area, because no other compensators are applied except the ones on the four segments crossing the quasi-branch-cuts. In this way, the unwrapping using the localized compensators can solve the problems of the choice of branch cuts in the path-following approaches. It can also solve the problems of the compensated area in the spreading singularity approaches.

C. Localized Compensator

As shown in the last example in Subsection 2.B, the localized compensator requires two conditions.

One is a source condition related to the number of singular points. The number of positive and negative singular points must balance each other out in the localized domain as

$$\sum_k m_k = 0. \qquad (10)$$

The decision of balanced singular points' groups, which is called "clustering," is shown in Section 3.

The other condition is the boundary condition. The localized compensator must vanish on every boundary segment, and this condition is provided instead.

To introduce the condition, it is convenient to define two unit vectors, $\hat{n}$ and $\hat{z}$, in addition to the $\hat{s}$; the $\hat{n}$ is the outward normal unit vector of the boundary, and the $\hat{z}$ is the perpendicular to the domain surface. The directions of these unit vectors satisfy $\hat{s} = \hat{z} \times \hat{n}$. By using these unit vectors, the integrand, $c \cdot \hat{s}$, of the last term in Eq. (9) is transformed as follows using Eq. (6):

$$c \cdot \hat{s} = -(\nabla \times A) \cdot (\hat{z} \times \hat{n}) = \hat{n} \cdot \nabla A_z, \qquad (11)$$

where $A_z = A \cdot \hat{z}$ and $\hat{z} \cdot \nabla \equiv 0$ for the two-dimensional problem is applied. The rightmost side of this equation shows a normal flux density of ∇A_z. Thus, the boundary condition for the localized compensator can be reduced to a Neumann condition:

$$\hat{n} \cdot \nabla A_z = 0. \qquad (12)$$

Meanwhile, a closed integral along any path C can be transformed by Stokes' theorem, Eq. (6), and Eq. (5) as follows:

$$\oint_C c \cdot \hat{s} \, dl = \int_S \nabla^2 A_z \, dS. \qquad (13)$$

A residue m_k at the point r_k in the right-hand side of Eq. (8) can be expressed by Dirac's delta function as follows:

$$m_k = \int_S m_k \delta(r - r_k) \, dS. \qquad (14)$$

Substituting Eqs. (13) and (14) into Eq. (8), and considering that the area S can be taken arbitrarily, we obtain that the A_z must satisfy the following Poisson's equation:

$$\nabla^2 A_z = -2\pi \sum_k m_k \delta(r - r_k). \qquad (15)$$

Consequently, the compensator shown in Eq. (11) is determined by the solution of Eq. (15) with the boundary condition given in Eq. (12) for the domain that is satisfying Eq. (10). The way to solve the A_z is shown in the Section 4.

Once the solution is found, compensator along every segment placed in the domain is evaluated as an integral of the flux density by Eq. (11). However, the outward normal vector $\hat{n}$ cannot be defined at the segment in the domain since the boundary loop is not defined. In this case, the normal vector can be replaced by $\hat{s} \times \hat{z}$, where $\hat{s}$ indicates the direction of the segment. As a result, the integral of the compensator is rewritten as below:

$$\int_{r_0}^r c \cdot \hat{s} \, dl = \int_{r_0}^r \hat{s} \times \hat{z} \cdot \nabla A_z \, dl. \qquad (16)$$
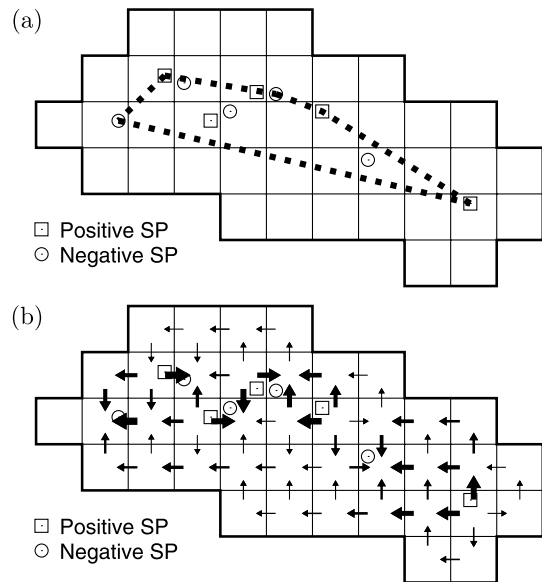

Fig. 2. Definition of local domain and flux density from singular points: (a) local domain including singular points, (b) flux distribution in the local domain. Outmost closed thick line is a boundary of the local domain, and the grids are segments of elementary loops. The dashed line in (a) represents a concave polygon that contains all singular points. The arrows in (b) are the flux density of which line width expresses the magnitude.

By using this relation, we can unwrap the wrapped phase by Eq. (9).

Figure 2 shows an example of a determined local region and an evaluated flux density distribution, whose detailed algorithms are shown in later sections. From the result in Fig. 2(b), it can be said that a large flux density distribution was found around singular points while it was comparatively small near the boundary.

3. Clustering

The clustering process generates zero-charged groups that are named "clusters," and they satisfy Eq. (10). Gutmann and Weber proposed a clustering algorithm to search a branch cut efficiently using a simulated annealing method [12]. Their clustering algorithm may be applicable to determine the local domain; however, it needs experiential parameters. We propose a new clustering algorithm without a use of experiential parameters.

As shown in Section 2, although the phase compensators defined in a cluster's region can regularize the singularity, it distorts the regular region. Therefore, the region of the cluster needs to be as small as possible.

If the measurement area is infinitely wide, all the zero-charged clusters can be found because the total numbers of them are always same. However, the actual area is finite. If the total numbers of positive and negative singular points in the area are different, we may not find the solution. Even when the total numbers are the same, a singular point to be coupled to the other singular point may be placed near the

border of the area, but it is outside the area. In this case, singular points in the area may become larger sized clusters. To avoid this problem, we introduce virtual singular points that are located outside the finite area [22].

The clustering procedure to find small sized clusters consists of two stages: cluster merging and cluster splitting. The cluster merging process usually increases the size of cluster, while the cluster splitting which reduces the size.

A. Cluster Merging Algorithm

1. Definitions of Singular Points, Virtual Singular Points, and Clusters

Singular points (SPs) are detected by Eq. (3), and every SP has a charge (residue) whose value is ± 1. The position of the SP is not in the center of the elementary loop by the algorithm of unconstrained SP positioning proposed in [22]. This positioning enables us to make an easy comparison of distances because the distance between an SP and another SP takes a continuous real number.

Every SP has a virtual SP (VSP) that is located at a symmetrical point to the nearest boundary of the two-dimensional phase map. In the following equations, $V(s_p)$ denotes the VSP corresponding to the pth SP, s_p. The VSP has an opposite charge to the corresponding SP:

$$Q(V(s_p)) = -Q(s_p), \qquad (17)$$

where the function $Q(\cdot)$ denotes the charge.

Every SP must belong to one of clusters; i.e., $s_{i,p} \in \mathcal{C}_i$, in which $\mathcal{C}_i$ shows the ith cluster and $s_{i,p}$ shows the pth SP in $\mathcal{C}_i$. In contrast, the VSP corresponding to the SP, $V(s_{i,p})$, can belong to the same cluster, but it can also become an unclustered VSP that does not belong to any clusters. When $v_{i,p}$ and $\bar{v}_{i,p}$ denote the clustered VSP and the unclustered VSP, respectively, the relations between the cluster and SPs are as follows:

$$\mathcal{C}_i = \{s_{i,p}, v_{i,p}\},$$
$$\{V(s_{i,p})\} = \{v_{i,p}\} + \{\bar{v}_{i,p}\},$$
$$s_{i,p} \in \mathcal{C}_i, v_{i,p} \in \mathcal{C}_i, \bar{v}_{i,p} \notin \mathcal{C}_i, \qquad (18)$$

where a pair of braces shows a population.

For each cluster, $\mathcal{C}_i$, a cluster charge can be defined as

$$Q_i \triangleq \sum_p Q(s_{i,p}) + \sum_{p'} Q(v_{i,p'}). \qquad (19)$$

The value of Q_i can be 0 or ± 1 during the cluster merging process, and it should become 0 finally.

The three distances can be also defined for each cluster. These distances are also shown in Fig. 3 as an example.

The first is the cluster distance, $L_{i,j}$, between two clusters, $\mathcal{C}_i$ and $\mathcal{C}_j$:
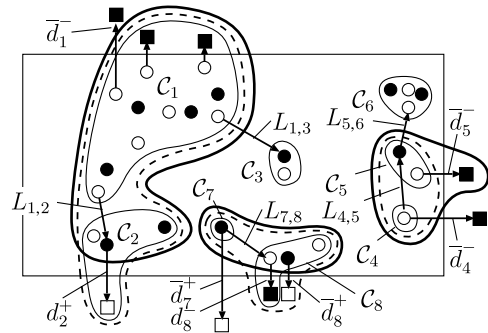

Fig. 3. Example of cluster merging. The rectangular frame shows the image domain. The circles are SPs, and the squares are VSPs. The open ones and filled ones indicate positive and negative charges, respectively. The closed curves with thin lines show the original clusters after several reputations. The new clusters shown as the closed curves with thick lines are formed by cluster merging. The closed curves with dashed lines are intermediate clusters. The arrows represent the typical linkages from host SPs to their partners.

$$L_{i,j} \triangleq \min_{p,q,Q=\pm 1} \left\{ \mathrm{Dist}\left(s_{i,p}^{+Q}, s_{j,q}^{-Q} \right) \right\}, \qquad (20)$$

where the function $\mathrm{Dist}(\cdot)$ returns the distance between two points, Q means the charge of $s_{i,p}$ [$Q = Q(s_{i,p}), s_{i,p} \in C_i$], and $s_{j,q}^{-Q}$ means the SP in other cluster j with the opposite charge [$Q(s_{j,p}) = -Q(s_{i,p})$].

The other two distances related to VSPs are defined as follows:

$$\bar{d}_i^{-Q_i} \triangleq \min_p \left\{ \mathrm{Dist}\left(s_{i,p}^{+Q_i}, \bar{v}_{i,p}^{-Q_i} \right) \right\}, \qquad (21)$$

$$d_i^{+Q_i} \triangleq \max_p \left\{ \mathrm{Dist}\left(s_{i,p}^{-Q_i}, v_{i,p}^{+Q_i} \right) \right\}. \qquad (22)$$

The $\bar{d}_i^{-Q_i}$ represents the shortest distance to an unclustered VSP. The distance is determined between possible pairs. Each pair consists of an SP in the considered cluster and an unclustered VSP corresponding to the SP. The charge of the SP is same as that of the cluster [$Q(s_{i,p}) = +Q_i$]. In contrast, the $d_i^{+Q_i}$ is the furthest distance to a clustered VSP. In this case, the charge of the SP is opposite to that of the cluster [$Q(s_{i,p}) = -Q_i$], and the VSP belongs to the same cluster. The superscript of both distances shown on the left-hand side shows the charge of the partner VSP. Similarly, the overline mark of the distance shows the attribute of the VSP.

2. Algorithm

The cluster merging algorithm has three major steps: coupling clusters, balancing clusters, and removing VSP pairs. These are repeated until charges of all the clusters vanish to make the size of clusters as small as possible. Once a cluster is changed, the quantities in Eqs. (19)–(22) are recomputed. In the algorithm, we call the cluster that merges another cluster "host cluster" and the merged cluster or

VSP "partner." The algorithm is shown below together with the descriptions of an example shown in Fig. 3, which is shown within a pair of round brackets.

Step 0: Initialization.

A single SP forms a cluster. All VSPs are assigned as unclustered VSPs. By this initialization, the charge of every cluster is ± 1.

Step 1: Coupling clusters.

From the charged clusters ($Q_i \neq 0$, in any i) (the candidates of hosts are $\{\mathcal{C}_1, \mathcal{C}_4, \mathcal{C}_7\}$ in the example), the cluster with the distance

$$L_{\mathrm{CP}} = \min_i \left\{ \min_j \{L_{i,j}\}, \bar{d}_i^{-Q_i} \right\}$$
$$\text{for } Q_i \neq 0, Q_j \neq Q_i, i \neq j, \quad (23)$$

is selected to be a host cluster, while the partner is either the cluster with different charge ($\mathcal{C}_j$ with $L_{i,j}$) or the unclustered VSP ($\bar{v}_{i,p}^{-Q_i}$ with $\bar{d}_i^{-Q_i}$) ($L_{\mathrm{CP}} = L_{1,2}$ in the example).
  If the partner is the cluster ($\mathcal{C}_j$), a new cluster, $\mathcal{C}_i$, is formed by merging as $\mathcal{C}_i := \{\mathcal{C}_i, \mathcal{C}_j\}$, where the symbol ":=" represents a substitution. (There are three intermediate clusters enclosed by the dashed curves for all candidates of hosts in the example.) The charge of the new cluster, Q_i, is 0 or ± 1 according to $Q_i := Q_i + Q_j$. This connection will not disconnect during the cluster merging algorithm.
  If the partner is the unclustered VSP ($\bar{v}_{i,p}^{-Q_i}$), it is merged to the host cluster as $\mathcal{C}_i := \{\mathcal{C}_i, \bar{v}_{i,p}^{-Q_i}\}$ (two short connections to the VSPs in $\mathcal{C}_1$ and the connection labeled d_8^- are results applied in the past iteration). In this case, since the partner has the opposite charge, the charge of the new cluster is balanced; i.e., $Q_i := 0$. As a result, the new cluster cannot become a host cluster in the next attempt, but it may become a partner cluster.

Step 2: Balancing cluster.

When the new coupled cluster has nonzero charge ($Q_i \neq 0$), the algorithm attempts removing or adding a VSP to balance the cluster charge. Both of these substeps can keep the growth of the cluster size low. If either of the following substeps to balance the charge is applied, the balanced cluster cannot become a host cluster in Step 1 in the future iterations.

Step 2-a: Removing a clustered VSP.

In the new cluster $\mathcal{C}_i$, if there is a clustered VSP with weaker coupling than the last coupling,

$$d_i^{+Q_i} > L_{\mathrm{CP}}, \quad (24)$$

the VSP, $v_{i,p}^{+Q_i}$ with $d_i^{+Q_i}$, is removed from the coupled cluster as $\mathcal{C}_i := \mathcal{C}_i - \{v_{i,p}^{+Q_i}\}$ (the connection labeled d_2^+).

Step 2-b: Adding an unclustered VSP.

If there is an unclustered partner VSP with stronger coupling than the last coupling,

$$\bar{d}_i^{-Q_i} < L_{\mathrm{CP}}, \quad (25)$$

the unclustered VSP, $\bar{v}_{i,p}^{-Q_i}$ with $\bar{d}_i^{-Q_i}$, is added to the cluster as $\mathcal{C}_i := \mathcal{C}_i + \{\bar{v}_{i,p}^{-Q_i}\}$. This substep increases the size of the cluster a little. However, since the new cluster cannot become a host, a chance to be coupled with other clusters is reduced, and this adding process might control the size of a cluster. (The connection with $\bar{d}_5^-$ of the cluster merged with $\mathcal{C}_4$ and $\mathcal{C}_5$. This addition can avoid a future link to $\mathcal{C}_6$.) This connection may be disconnected by other steps in a future iteration (the connections to clustered VSPs in the original $\mathcal{C}_2$ and $\mathcal{C}_8$ were established by this substep in the past iterations, but they are disconnected).

Step 3: Removing VSP pairs.

Among the possible pairs of VSPs with opposite charges, $v_{i,p}^+$ and $v_{i,q}^-$, if the distance between pairs is shorter than the sum of distances to the corresponding SPs,

$$\mathrm{Dist}(v_{i,p}^+, v_{i,q}^-) < \mathrm{Dist}(s_{i,p}^-, v_{i,p}^+) + \mathrm{Dist}(s_{i,q}^+, v_{i,q}^-), \quad (26)$$

both the VSPs do not play a role to balance the charge of cluster. These VSPs are disconnected from the cluster to reduce the size of cluster; i.e., $\mathcal{C}_i := \mathcal{C}_i - \{v_{i,p}^+, v_{i,q}^-\}$ (two connections in the cluster merged with $\mathcal{C}_7$ and $\mathcal{C}_8$).

  The processes from Step 1 to Step 3 are repeated until no charged clusters can be found.

B. Cluster Splitting Algorithm

Since clusters can be coupled with zero-charged clusters in the cluster merging algorithm, the cluster size increases (except for the removal of some VSPs). In these clusters, some clusters can be split to reduce the size. An example of the splittable cluster is shown in Fig. 4. The progression of the cluster creation by the cluster merging algorithm is shown in Fig. 4(a). The cluster can be split into two clusters, and their charges are zero as shown in Fig. 4(b).
  A linkage is defined as a connection between two opposite charged SPs that include VSPs as well as real SPs. The length of the linkage is determined in the cluster merging algorithm to find a cluster to couple with. The cluster splitting algorithm shown here attempts to cut off some of the linkages. Each cluster has one or more linkages and two or more end SPs. Each end SP has a single linkage.
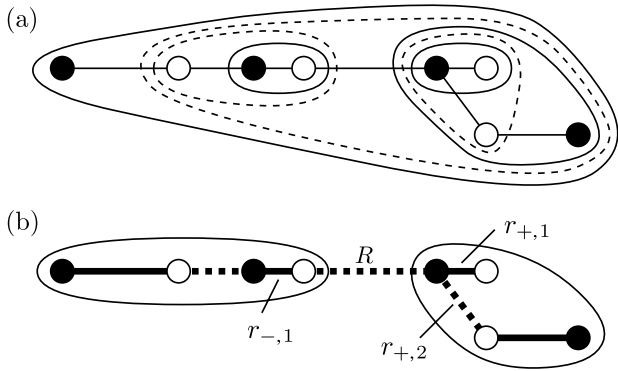
Fig. 4. Schematics of cluster splitting: (a) an example of cluster merging progress and (b) cluster splitting. The open circles and filled circles are SPs (or VSPs) with positive charges and those with negative ones, respectively. The lines between SPs are their linkages. The closed curves with solid and dashed lines represent the zero-charged clusters and the charged clusters, respectively. The clusters in (a) are those after every stage, and the outmost cluster is the final result of the cluster merging process. The clusters split into two shown in (b) are formed by the cluster splitting algorithm. In (b), dashed lines and solid lines indicate the splittable linkages and the unsplittable linkages, respectively.

The linkage has an attribute which is either "splittable" or "unsplittable." When the cluster is divided at the linkage connecting with one of the end points, one of the divided clusters has the sole end point with nonzero charge. Therefore, this linkage is not unsplittable. All linkages next to the unsplittable linkage are splittable linkages. The cluster is temporarily divided at the splittable linkages. Applying the same procedures to the new clusters, we can determine the attributes of all linkages.

The original cluster can be divided at the splittable linkage, but only under certain conditions. The length of the splittable linkage is compared with that of the other linkages connecting to the two SPs at the both ends of the splittable linkage. The linkage is divided if all the lengths are shorter than the length of the splittable linkage. In the example shown in Fig. 4(b), there are three splittable linkages; however, only one linkage is disconnected. The right horizontal linkage with the length R is splittable because all lengths of $r_{-,1}$, $r_{+,1}$, and $r_{+,2}$ are shorter than R.

4. Flux Satisfying Poisson's Equation

For each cluster determined by the algorithm shown in the Section 3, the domain to apply the local compensator is defined as one pixel (elementary loop) width wider area than the region of the convex shaped area that contains all SPs in the balanced cluster. The boundary of the domain is set on the outermost segments; an example is shown in Fig. 2(a).

As shown in Eq. (11), the compensator for phase unwrapping is equivalent to the flux density of ∇A_z when A_z satisfies a Poisson's equation [Eq. (15)] with the boundary condition given by the Neumann condition with zero-flux density [Eq. (12)].

To solve A_z, any field solver may be applicable. In this study, boundary element method (BEM) [26] is adopted as a basic solver. In the BEM, the unknown boundary values at the boundary nodes (A_z) are solved as a set of discretized boundary integral equations for the all boundary nodes. After solving this set of equations, all boundary values, A_z and ($\nabla A_z \cdot \hat{\boldsymbol{n}}$), are determined. Internal flux density at arbitrary points can be evaluated as hypersingular integrals (e.g., [27–29]) from all boundary values. Several integration points on a segment are set to estimate the integral of the flux density on each segment. However, when the point to estimate the field is located near the source points, which correspond to the SPs, the BEM has a large computational error.

The following flux conservation law for every elementary loop cannot be satisfied due to the error:

$$\oint_c \nabla A_z \cdot \hat{\boldsymbol{n}} \mathrm{d}l = -2\pi \sum_k \int_S m_k \delta(\boldsymbol{r} - \boldsymbol{r}_k) \mathrm{d}S, \qquad (27)$$

which is derived from Eq. (15) using the Gauss' divergence theorem. To reduce this error, we apply a singular value decomposition (SVD) method to find a minimum-norm solution. We define the error vector on the jth segment in the kth elementary loop, $\boldsymbol{e}_{k,j}$, as a difference between the gradient computed by the BEM, $(\nabla A_z)'_{k,j}$, and the gradient satisfying the flux conservation law, $(\nabla A_z)_{k,j}$:

$$\boldsymbol{e}_{k,j} = (\nabla A_z)'_{k,j} - (\nabla A_z)_{k,j}. \qquad (28)$$

The flux conservation law shown in Eq. (27) for the elementary loop k is rewritten as

$$\sum_{j=1}^4 ((\nabla A_z)'_{k,j} - \boldsymbol{e}_{k,j}) \cdot \hat{\boldsymbol{n}}_{k,j} = -2\pi m_k. \qquad (29)$$

The number of equations is identical to that of loops, N_l, and the number of unknown variables of $\boldsymbol{e}_{k,j} \cdot \hat{\boldsymbol{n}}_{k,j}$ is $4N_l$ because each loop has four segments. However, the $\boldsymbol{e} \cdot \hat{\boldsymbol{n}}$ is known as zero on the boundary segments of which the number is N_b. Furthermore, since every internal segment belongs to two loops, the error vectors in these two loops can be defined by a vector on a segment,

$$\boldsymbol{e}_{k,j} = \boldsymbol{e}_{k',j'} = \boldsymbol{e}_i, \qquad (30)$$

where the two subscript pairs of k,j and k',j' indicate the same segment i. Thus, the number of unknowns is reduced to that of internal segments; i.e., $N_s = (4N_l - N_b)/2$. In contrast to the error vector, two direction vectors, $\hat{\boldsymbol{n}}_{k,j}$ and $\hat{\boldsymbol{n}}_{k',j'}$, on the segment i have a different direction. When we introduce a new unit vector, $\hat{\boldsymbol{d}}_i$, that is identical to either $\hat{\boldsymbol{n}}_{k,j}$ or $\hat{\boldsymbol{n}}_{k',j'}$, the normal unit vector can be defined as

$$\hat{\boldsymbol{n}}_{k,j} = d_{k,i}\hat{\boldsymbol{d}}_i, \qquad (31)$$

where $d_{k,i}$ can take either ± 1, depending on the loop as well as the segment. Thus, Eq. (29) can be transformed to the following matrix form:

$$\mathbf{De} = \mathbf{r}, \tag{32}$$

$$(\mathbf{D})_{k,i} = d_{k,i}, (\mathbf{e})_i = \hat{\boldsymbol{d}}_i \cdot \boldsymbol{e}_i,$$
$$(\mathbf{r})_k = 2\pi m_k - \sum_i d_{k,i} \hat{\boldsymbol{d}}_i \cdot (\nabla A_z)'_i. \tag{33}$$

In Eq. (32), the $\mathbf{D}$ is an N_l-by-N_s matrix. In most clustered domains, the relation between the dimensions of the matrix is given as $N_l < N_s$, except in a few cases in which the domain consists of one-dimensionally aligned loops or a 2-by-2 aligned loop. Therefore, the set of equations is a rank-deficient, underdetermined system of linear equations that cannot be solved in an ordinal way. However, since the solution list, $\mathbf{e}$, is the list of errors that should be small, the following condition can be imposed:

$$\text{minimize} \sum_i |(\mathbf{e})_i|^2. \tag{34}$$

To solve Eq. (32) with this condition, we used an SVD routine provided by LAPACK [30]. The flux is updated by the error

$$(\nabla A_z)_{k,j} = (\nabla A_z)'_{k,j} - \boldsymbol{e}_{k,j}. \tag{35}$$

An example of the ∇A_z is shown in Fig. 2(b).

After the ∇A_z is obtained, the compensator for the segment is evaluated by Eq. (16). In the case where a segment belongs in several cluster domains, the compensator is accumulated as

$$\boldsymbol{c} = \sum_m \boldsymbol{c}_m, \tag{36}$$

where $\boldsymbol{c}_m$ is the compensator to the segment of the mth domain.

5. Numerical Results of Phase Unwrapping for Noisy Data

In this section, three examples of phase unwrapping for noisy wrapped phase maps are presented. One is a simulation using a phase map where the phase is known to evaluate the accuracy of the algorithms quantitatively. The other two are unwrapping for actual wrapped data obtained by experiments to demonstrate the applicability of proposed phase unwrapping algorithm.

A. Unwrapping Simulation for Known Phase Map

To evaluate the accuracy of the phase unwrapping using a localized compensator (LC), we provide a known phase distribution that is not wrapped. A wrapped phase map that is an input for phase unwrapping algorithms is computed from the known
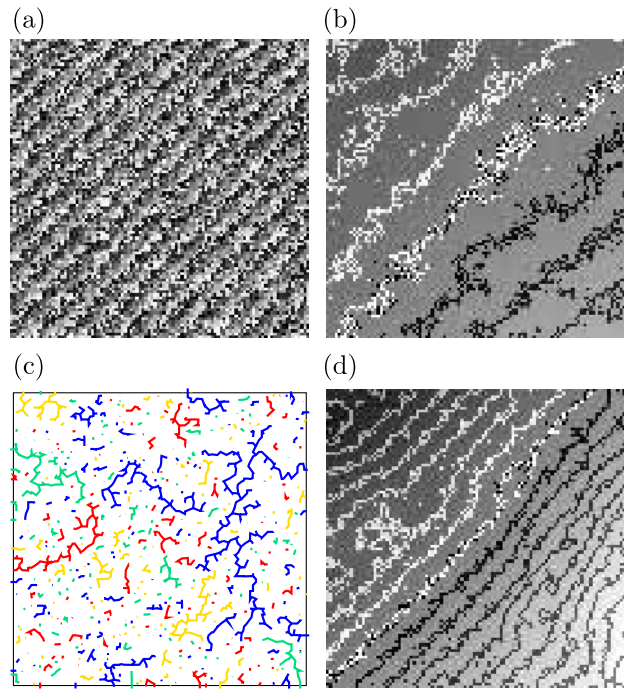

Fig. 5. (Color online) Phase unwrapping simulation: (a) original wrapped phase map, (b) unwrapped phase map by the LS-DCT method, (c) connections of the clustered tree, (d) unwrapped phase map by the method using an LC.

phase map. The unwrapped results are compared with the known phase map.

The prepared original phase map is a noisy phase map with a constant gradient; the image area has 100×100 pixels, the gradient is $(0.1, -0.1)$ cycle/pixel, and the noise has a normal distribution with 0.20 cycle standard deviation. In this phase map, there are 1033 positive SPs and 1031 negative SPs; the sum of them exceeds 20% of the number of all nodes. This original map with unbounded value is wrapped as input data for phase unwrapping. Figure 5 shows the wrapped phase map together with the unwrapped results by the least-square with discrete cosine transform (LS-DCT) method [20] and by the proposed method using LC. In the unwrapped results, contour lines have been drawn with the interval of one cycle. Figure 5(c) shows a clustered tree of SPs in the LC method. Counting the number of contour lines in the unwrapped results, we can find that the phase gradient in the result by the LS-DCT method is smaller than that of the original phase map and that by the LC method approaches to that of the original one. However, there is large distortion of the unwrapped phase in the LC method. It is found from the clustered tree that the distorted regions are corresponding to the regions around large clusters.

Table 1 provides a quantitative comparison among five methods: Goldstein's path-following method [7], the LS-DCT method [20], the method using the RC with VSPs and unconstrained SP positioning [22], the coupling method with the RC and direct

Algorithm	RMS[a] of $\phi - \phi^{\mathrm{orig}}$	Gradient $(\bar{\phi}_x, \bar{\phi}_y)$	Ratio of Gradient $(\bar{\phi}_x/\bar{\phi}_x{}^{\mathrm{orig}}, \bar{\phi}_y/\bar{\phi}_y{}^{\mathrm{orig}})$	RMS[a] of $\phi - \bar{\phi}$
Standard deviation of noise: 0.15 (cycle) $[N(s^+) = 453, N(s^-) = 456]$				
Original (ϕ^{orig})	—	(0.1000, −0.1000)	(—, —)	0.1491
Goldstein	0.7201	(0.0892, −0.0826)	(0.892, 0826)	0.4250
LS-DCT	1.0893	(0.0742, −0.0731)	(0.742, 0.730)	0.1790
RC	0.4077	(0.0912, −0.0899)	(0.912, 0.899)	0.1656
RC&DC	0.2433	(0.0949, −0.0946)	(0.949, 0.946)	0.1642
LC (proposed)	0.0704	(0.1000, −0.1000)	(1.000, 1.000)	0.1338
Standard deviation of noise: 0.20 (cycle) $[N(s^+) = 1033, N(s^-) = 1031]$				
Original (ϕ^{orig})	—	(0.1001, −0.1001)	(—, —)	0.1989
Goldstein	2.0347	(0.0733, −0.0538)	(0.733, 0.538)	1.3259
LS-DCT	2.5542	(0.0368, −0.0389)	(0367, 0.389)	0.2389
RC	1.2604	(0.0708, −0.0689)	(0.707, 0.689)	0.2419
RC&DC	1.0694	(0.0754, −0.0740)	(0754, 0739)	0.2622
LC (proposed)	0.6545	(0.1034, −0.0879)	(1.034, 0878)	0.5412

[a]RMS indicates a root mean square.

compensator (RC&DC) [23], and the LC method. The table shows the accuracy in two cases where the standard deviation of noise is 0.15 cycles and 0.20 cycles. The first column shows a root mean square (RMS) of the difference between the unwrapped phase, ϕ, and the original one, ϕ^{orig}. The components of gradient vector in the second and the third columns are obtained by fitting the unwrapped phase to a planar function: $\bar{\phi}(\boldsymbol{r}) = \nabla\bar{\phi} \cdot \boldsymbol{r} + \bar{\phi}_0$. Accuracy for each component of the $\nabla\bar{\phi}$ is shown in the fourth and the fifth columns as a ratio between the unwrapped phase and the original phase. They show the global difference due to singularity spreading. The last column shows an RMS of the difference between ϕ and $\bar{\phi}$, which means the local difference due to phase unwrapping. This RMS is not equal to zero even in the original data because the original data contain the noise with the specified standard deviation. In terms of accuracy of the gradient, the LC method is superior to the others in both cases of noise with 0.15 and 0.20 cycles. Especially in the case of 0.15, the errors of the gradient in the LC method are negligibly small. In terms of the RMS of $\phi - \bar{\phi}$, the LC has the nearest value in the case of noise with 0.15 cycles, while in the case of 0.20 it is not the best result. This result also supports the above discussion of the result shown in Fig. 5.

B. Unwrapping of Interferometric Synthetic Aperture Radar Data

Figure 6 shows phase unwrapping of the data obtained using interferometric synthetic aperture radar (IFSAR) [31]. The wrapped data contain noisy regions due to decorrelation of the interferometer. A distribution of clustered connections of SPs is shown in Fig. 6(b).

The unwrapped results using the RC [Figs. 6(c) and 6(c')] and LC [Figs. 6(d) and 6(d')] can be compared with the original wrapped phase [Fig. 6(a)]. A reference point is the top left point on each image. At the reference point, the unwrapped phases in both the methods are identical to the wrapped phase.

Therefore, in an ideal unwrapping, phase jumping positions where the intensity is rapidly changing in the wrapped phase map are identical to the
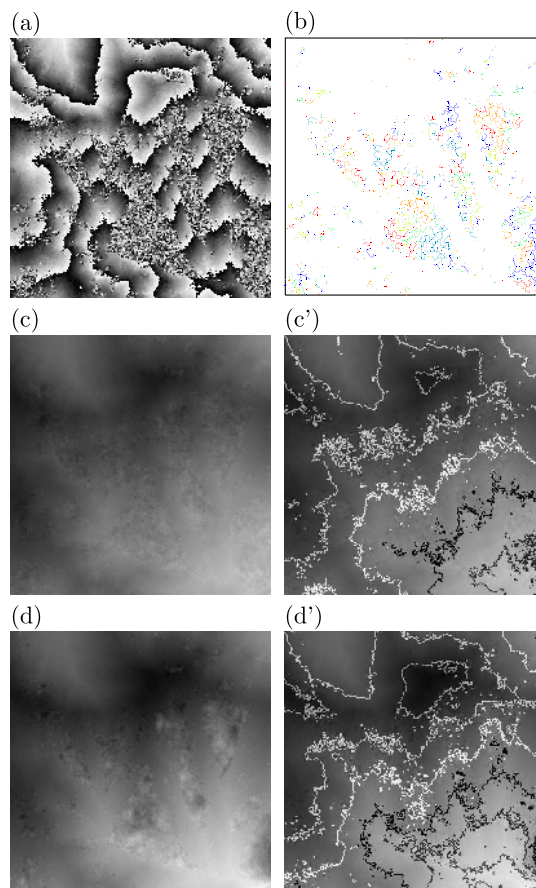

Fig. 6. (Color online) Unwrapping an experimental IFSAR phase: (a) a wrapped phase map (512 × 512) from [31] (copyright 1998 by John Wiley and Sons, Inc. Reproduced with permission of John Wiley and Sons, Inc.), (b) the clustered trees, (c) the unwrapped phase by the method using the RC, (d) the unwrapped phase by the method using an LC. The images (c') and (d') are the unwrapped phase with contour lines where the step is 2π radian.

positions of the contour in the unwrapped phase map. In Fig. 6(d′), the positions of contour lines are almost same to the positions of phase jumps. In contrast, it is found that the number of contours in Fig. 6(c′) is smaller than that of Fig. 6(d′). This characteristic is similar to the example in Subsection 5.A. In addition, although an unwrapped result within the noisy region is meaningless in this IFSAR data, when we examine the noisy regions, it is found that variance of the unwrapped result using the RC is smaller than the result using the LC. The reason is still the affected region of the compensator. Since the number of the compensators in the LC is less than that in the RC, the averaging effect of the LC is smaller than the RC.

C. Unwrapping of Optical Interferometric Data

Figure 7 demonstrates phase unwrapping for actual experimental data to measure a phase shift caused by candle flame. The setup to measure the fringe pattern is shown in [22]. The fringe pattern, $I(r)$, obtained using an interferometer is shown in Fig. 7(a). The wrapped phase was computed from the fringe pattern by applying the Fourier domain method [1–3] as below. The fringe pattern is expressed as a real valued function, which can be rewritten as the following form using two complex valued terms:

$$I(r) = I_0 + \frac{I_1}{2}(e^{i(\phi(r)+k_{bg}\cdot r)} + e^{-i(\phi(r)+k_{bg}\cdot r)}), \quad (37)$$

(a) Fringe pattern
(b) Wrapped

(c) LS-DCT
(d) RC
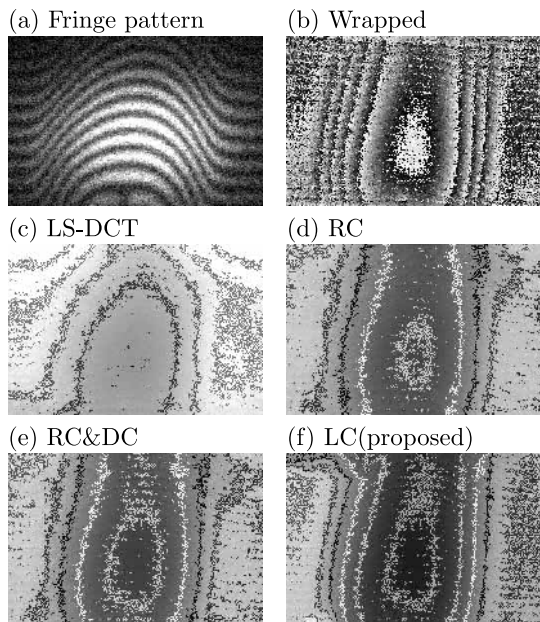

(e) RC&DC
(f) LC(proposed)

Fig. 7. Estimation of phase shift due to candle flame: (a) fringe pattern obtained by a Mach–Zehnder interferometer with a candle flame; (b) wrapped phase obtained from the fringe pattern by a Fourier transformed filter and by background phase shifting; (c)–(f) unwrapped phase distributions with different methods; in each unwrapped result, the reference point is positioned at the bottom left corner at which the unwrapped phases by all methods are same. The candle has a core at the bottom center in each figure.

where k_{bg} is the wavenumber vector of the background fringe that is determined by the angle between the object wave without the object and the reference wave and $\phi(r)$ is the added phase by the object. The Fourier transform of the $I(r)$ has three peaks in the Fourier domain corresponding to each term of the right-hand side. One is the peak corresponding to the constant component in the real domain, which appears as a Dirac's delta function at the origin in the Fourier domain. The other two are twin spectra; they have symmetry about the origin, and they distribute around $\pm k_{bg}$. The complex distribution of $\exp\{i(\phi(r) + k_{bg} \cdot r)\}$ can be extracted by two steps: filtering out two peaks around the origin and one of the twin peaks, and inverse Fourier transform. Moreover, the background component can be canceled by phase subtracting $k_{bg} \cdot r$ since the k_{bg} is estimated from the spectrum in the Fourier domain. Taking the angle of the complex function, we can obtain the wrapped phase shown in Fig. 7(b). The wrapped phase map includes about 3000 SPs within the image area of 256 × 170 pixels; it reaches almost 7%. The unwrapped results by using four approaches are shown in Fig. 7(c)–7(f): the LS-DCT method, the method using the RC, the coupling method with the RC&DC, and the LC. The accuracy of phase unwrapping methods can be evaluated by comparing the shape of phase discontinuity in the wrapped difference and the shape of contour lines in the unwrapped phases. As in the previous subsections, it is found that the accuracy of LC is superior to the other methods.

The computational time for each phase unwrapping algorithm is measured with a PC including an Intel Core 2 DUO CPU with 2.13 GHz clock in a single CPU operation mode. It takes 0.7 s, 32 s, 19 s, and 83 s with the LS-DCT method, the RC, the RC&DC, and the LC, respectively. In the case of the LC, nearly 90% of the computational time is spent solving flux by the BEM and fixing the error by the method using SVD shown in Eq. (32), most of which was devoted to large clusters. This is the problem of the LC method.

6. Conclusion

To implement more accurate phase unwrapping for noisy wrapped phase maps, we propose a new method that uses the LC. The method is one of the singularity-spreading phase unwrapping methods, such as the least-square method, the singularity spreading, and the RC. The difference between the proposed method and the past methods in the singularity-spreading type is just the area they use to spread the singularity. Since the area regularized by the LC is the local area that contains SPs, the regular area not containing the SPs is not distorted. In terms of the accuracy, the method using the LC is superior to the other methods. However, it has a drawback in that the computation time is longer than the other methods in the same type.

References

1. M. Takeda, H. Ina, and S. Kobayashi, "Fourier-transform method of fringe-pattern analysis for computer-based topography and interferometry," J. Opt. Soc. Am. **72**, 156–160 (1982).

2. K. E. Perry, Jr. and J. McKelvie, "A comparison of phase shifting and Fourier methods in the analysis of discontinuous fringe patterns," Opt. Lasers Eng. **19**, 269–284 (1993).

3. E. Cuche, P. Marquet, and C. Depeursinge, "Spatial filtering for zero-order and twin-image elimination in digital off-axis holography," Appl. Opt. **39**, 4070–4075 (2000).

4. J. H. Bruning, D. R. Herriott, J. E. Gallagher, D. P. Rosenfeld, A. D. White, and D. J. Brangaccio, "Digital wavefront measuring interferometer for testing optical surfaces and lenses," Appl. Opt. **13**, 2693–2703 (1974).

5. B. Breuckmann and W. Thieme, "Computer-aided analysis of holographic interferograms using the phase-shift method," Appl. Opt. **24**, 2145–2149 (1985).

6. J. Jiang, J. Cheng, Y. Zhou, and G. Chen, "Clustering-driven residue filter for profile measurement system," J. Opt. Soc. Am. A **28**, 214–221 (2011).

7. R. M. Goldstein, H. A. Zebker, and C. L. Werner, "Satellite radar interferometry: two-dimensional phase unwrapping," Radio Sci. **23**, 713–720 (1988).

8. J. M. Huntley, "Noise-immune phase unwrapping algorithm," Appl. Opt. **28**, 3268–3270 (1989).

9. J. R. Buckland, J. M. Huntley, and S. R. E. Turner, "Unwrapping noisy phase maps by use of a minimum-cost-matching algorithm," Appl. Opt. **34**, 5100–5108 (1995).

10. R. Cusack, J. M. Huntley, and H. T. Goldrein, "Improved noise-immune phase-unwrapping algorithm," Appl. Opt. **34**, 781–789 (1995).

11. M. Costantine, "A novel phase unwrapping method based on network programming," IEEE Trans. Geosci. Remote Sens. **36**, 813–821 (1998).

12. B. Gutmann and H. Weber, "Phase unwrapping with the branch-cut method: clustering of discontinuity sources and reverse simulated annealing," Appl. Opt. **38**, 5577–5593 (1999).

13. S. A. Karout, M. A. Gdeisat, D. R. Burton, and M. J. Lalor, "Two-dimensional phase unwrapping using a hybrid genetic algorithm," Appl. Opt. **46**, 730–743 (2007).

14. D. L. Fried, "Least-square fitting a wave-front distortion estimate to an array of phase-difference measurements," J. Opt. Soc. Am. **67**, 370–375 (1977).

15. R. H. Hudgin, "Wave-front reconstruction for compensated imaging," J. Opt. Soc. Am. **67**, 375–378 (1977).

16. B. R. Hunt, "Matrix formulation of the reconstruction of phase values from phase differences," J. Opt. Soc. Am. **69**, 393–399 (1979).

17. D. C. Ghiglia and L. A. Romero, "Direct phase estimation from phase differences using fast elliptic partial differential equation solvers," Opt. Lett. **14**, 1107–1109 (1989).

18. H. Takajo and T. Takahashi, "Least-squares phase estimation from the phase difference," J. Opt. Soc. Am. A **5**, 416–425 (1988).

19. H. Takajo and T. Takahashi, "Noniterative method for obtaining the exact solution for the normal equation in least-squares phase estimation from the phase difference," J. Opt. Soc. Am. A **5**, 1818–1827 (1988).

20. D. C. Ghiglia and L. A. Romero, "Robust two-dimensional weighted and unweighted phase unwrapping that uses fast transforms and iterative methods," J. Opt. Soc. Am. A **11**, 107–117 (1994).

21. R. Yamaki and A. Hirose, "Singularity-spreading phase unwrapping," IEEE Trans. Geosci. Remote Sens. **45**, 3240–3251 (2007).

22. S. Tomioka, S. Heshmat, N. Miyamoto, and S. Nishiyama, "Phase unwrapping for noisy phase maps using rotational compensator with virtual singular points," Appl. Opt. **49**, 4735–4745 (2010).

23. S. Heshmat, S. Tomioka, and S. Nishiyama, "A reliable phase unwrapping algorithm based on rotational and direct compensators," Appl. Opt. **50**, 6225–6233 (2011).

24. D. J. Bone, "Fourier fringe analysis: the two-dimensional phase unwrapping problem," Appl. Opt. **30**, 3627–3632 (1991).

25. P. M. Morse and H. Feshbach, *Methods of Theoretical Physics* (McGraw-Hill, 1953), pp. 52–54.

26. C. A. Brebia and S. Walker, *Boundary Element Techniques in Engineering* (Newnes-Butterworths, 1980).

27. S. Tomioka and S. Nisiyama, "Analytical regularization of hypersingular integral for Helmholtz equation in boundary element method," Eng. Anal. Bound. Elem. **34**, 393–404 (2010).

28. M. Arai, T. Adachi, and H. Matsumoto, "Highly accurate analysis by boundary element method based on uniform gradient condition," Trans. Jpn. Soc. Mech. Eng. A **61**, 161–168 (1995), in Japanese.

29. M. Guiggiani, G. Krishinasamy, T. J. Rudolphi, and F. J. Rizz, "A general algorithm for the numerical solution of hypersingular boundary integral equations," Trans. ASME **59**, 604–614 (1992).

30. E. Anderson, Z. Bai, C. Bischof, J. Demmel, J. Dongarra, J. Du Croz, A. Greenbaum, S. Hammarling, A. McKenney, S. Ostrouchov, and D. Sorensen, *LAPACK Users' Guide* (Society for Industrial and Applied Mathematics, 1992).

31. D. C. Ghiglia and M. D. Pritt, *Two-Dimensional Phase Unwrapping: Theory, Algorithms, and Software* (Wiley, 1998).